HEFAT 2008
6th International Conference on Heat Transfer, Fluid Mechanics and Thermodynamics
30 June to 2 July 2008
Pretoria, South Africa
Paper number: MA1

# Experimental Analysis and Simulation of Cavitating Throttle Flow

Dr. Alexander Morozov, AVL List GmbH, A-8020 Graz
Dr. Uwe Iben, Robert Bosch GmbH, Dept. CR/ARH, D-70049 Stuttgart

April 25, 2008

**Abstract**

While there exist many papers on cavitating flow on large smooth streamlined bodies, very small geometries are less studied. In this paper, optical measurement techniques for local density and velocity distributions are used to analyze cavitating flow in micro geometries at the critical cavitation point. The experimental results are used for validation of the commercial CFD code ANSYS CFX-11. The consensuses as well as differences of results are analyzed and discussed.

## 1 Introduction

Cavitating flow often occurs in hydraulic systems and can not be avoided due to system requirements such as closing times of valves or fast changes of system pressure levels. It can lead to noise or damage of system components. Frequently, since cavitation can not be avoided, it has to be controlled in order to guarantee a long life time of hydraulic systems with low noise levels. Cavitation leads to a highly transient flow with large local pressure fluctuations due to the collapsing of vapor bubbles, the change of local speed of sound and change of local mixture viscosity. The enormous change of the fluid properties due to cavitation has influence on the hydraulic properties of flow systems, such as eigenfrequencies or valve characteristics. Simulation can help to understand properties of cavitating flow such as properties of valves and other system components in order to optimize hydraulic properties. The simulation is based on models which have to be validated by complex experiments. In order to generate meaningful validation data for cavitating flow, pressure, velocity, temperature and void fraction fields have to be measured, which is a challenge considering the small size of the technical devices. Most studies on cavitating flow have been made on large, smooth and streamlined bodies. The basic cavitation characteristics in these cases are fairly well understood. Shear flow cavitation as well as cavitation as a result of laminar separation are of high practical importance. The understanding of cavitation inception has not been extensively studied because of several analytical and experimental complications. First, shear flow cavitation in combination with laminar separation flow in throttles can only be observed on very small time scales and requires high-quality measurement techniques. Second, the underlying single phase flow has complex flow structures and local flow values can only be measured with special optical measurement techniques. The mean pressure variations in a turbulent flow are often small, but the instantaneous peak local pressures can vary significantly from the mean value, cf. [11].
Rectangle throttles are used to study cavitating flow. Cavitation occurs at two geometrical regions of the throttle. Firstly close the inlet at the shear layer of the laminar separation bubble, secondly in the shear layer of the wake flow behind the throttle. The shear layer cavitation is strongly connected with turbulent structures which have small geometrical sizes and time scales.
This paper deals with the experimental analysis of density and local velocity measurements for cavitating throttle flow with small geometrical size. The data are used to study the properties of turbulence and cavitation models of the commercial CFD code ANSYS CFX-11.

The paper is organized as follows: Section 2 contains the complete description of the experimental facilities. The optical measurement techniques are outlined in Section 3. The experimental analysis of local density distributions as well as of velocity measurement techniques are described in Section 4. Applied CFD methods are detailed in Section 5, where the simulation results are compared with the experimental data. A summary is given at the end of the paper.

## 2 Experimental facilities

A complete hydraulic system consisting of a fluid tank, a high pressure pump, a metal throttle and a cooling system for fluid was installed. The metal throttle is sandwiched between two sapphire windows. The optical access allows visualization of the fluid flow with high pressure differences (up to 1000 bar). The tested geometries — a throttle with a sharp inlet called I-channel and a throttle with a rounded inlet called Y-channel[1] — are included in a steel plate with a thickness of 0.3 mm. The test facility and the geometrical dimensions of the throttle are presented in Fig. 1. The flow enters and leaves the domain perpendicular to the steel plate plane with low fluid velocity due to the large entrance and exit diameters. The flow path is marked with a light blue line. The installed hydraulic system guarantees a variable inlet pressure (up to 1000 bar) with pressure fluctuations smaller than 1 bar. The back flow system contains a damping container with back flow pressure fluctuations of ± 1 bar in order to avoid reflections of pressure waves generated by cavitation. The installed cooling system guarantees a fixed inlet temperature. The back flow temperature depends on the pressure differences on the throttle. The inlet and outlet pressures are measured by Kistler pressure sensors with a sampling rate of 50 kHz. The temperatures at inlet and outlet are measured by PT100 elements. The integral mass flow is measured by a Coriolis mass flow meter. Working fluid is commercially available Diesel fuel. The experimental results were not influenced by small variations of Diesel fuel properties such as component composition, viscosity, and density from one manufacturer to another. Additional details about the hydraulic equipment are described in [13, 14, 6, 15].

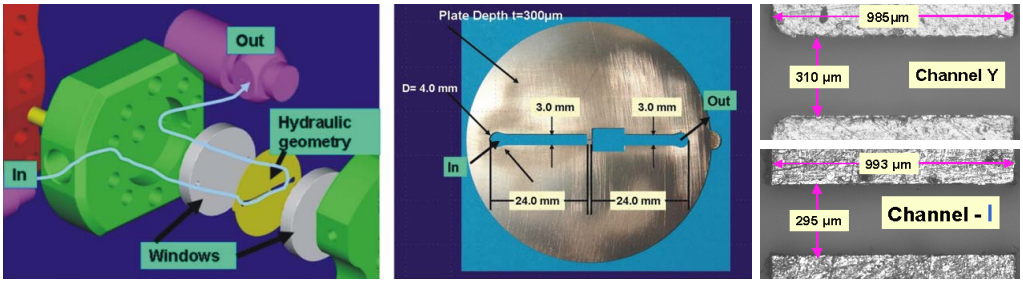


Figure 1: (Left) Test facility and throttle with optical access; (Right) Plate with throttle geometry, plate depth 300 µm.

## 3 Optical measurement techniques

The following local flow field parameters were determined:

1. Distribution of liquid–vapor areas in cavitating flows (using light transmission measurements).

2. Pressure and temperature field distributions in throttle flows (using interferometry): mean local values and fluctuations (standard deviation and single-shot difference from mean value).

[1]The Y-channel has nearly the same geometrical sizes than the I-channel and additionally a rounded inlet with a radius of 100 µm

3. Local velocity profiles and local velocity fluctuations at fixed geometrical positions (using Laser Induced Fluorescence – LIF).

4. Fluctuation parameters: localization and pressure values (using differential distributions with digital interferometry).

The optical measurements were supported by the simultaneous hydraulic measurements of inlet and outlet pressures denoted by $P_{in}$ and $P_{out}$ , temperatures $T_{in}$ and $T_{out}$, and integral mass-flow using corresponding sensors.
The optical part consisted of the imaging system with ≈10 times optical magnification in combination with digital cameras PCO SensiCam and DiCAM and a set of light sources, i.e. flash lamp, continuous wave He-Ne (633 nm) and pulsed KrF (248 nm) excimer lasers. The system supported an image size 1280x1024 pix with resolution up to 0.8 µm/pix and image recording times 10 ns (KrF-laser and DiCAM-camera for velocity measurements), 100 ns (flash lamp and SensiCam-camera for cavitation and turbulence visualization) and 400 ns (He-Ne-laser and SensiCam for density distribution measurements with interferometry). A Mach-Zehnder interferometer was used for density measurements and UV-optics and slit were applied during velocity measurements with laser induced fluorescence (LIF). An interferometrical technique was applied for measurements of density distributions of high pressure diesel flows in an optical throttle. The single image phase distribution accuracy was about 0.3 radian, that corresponds to $\lambda/20$. This value, in turn, supports an accuracy of local pressure measurements at the level P = ± 3 bar, and temperature T = ± 0.3 °C. These results were obtained by several optimizations in hardware: adaptation of a Mach-Zehnder interferometer for the specific task, application of digital cameras and digital optical processing employing two-dimensional Fourier transform. These options allow the study of small local flow features, such as turbulence, boundary and shear layers and to realize high accuracy of local pressure measurements in narrow (about 100 µm) channels.
A new method was applied for liquid high-pressure diesel flow velocity measurements. A short UV laser pulse prepared as a spatially narrow light sheet is absorbed by diesel. The temporally delayed LIF-signal is recorded using a digital camera with a definite temporal gate. The flow motion during temporal delay between excitation and recording produces a spatial shift of LIF-signal, which can be measured optically and thus contains information about flow velocities. The measurement error is estimated at 3% inside the velocity range of 50 m/s to 500 m/s. The measured mean velocity values display a good agreement with calculated Bernoulli velocities.
Diesel fuel has strong absorption at 248 nm, and practically 100% of light is absorbed within a 0.1 mm layer of diesel fuel. Additional measurements of the spatial decays of LIF-signal in the direction perpendicular to the pumping direction were made. These measurements show that LIF-intensity has an exponential decay with intensity maximum at the glass wall and a penetration half width of about 15 µm. As long as the boundary layer of the flow is less than this 15 µm, the LIF profiles show the main bulk flow velocity. This was found near the throttle entrance and was proved with mass flow measurements under stationary conditions. The thickness of boundary layer depends on Reynolds number[2] and grows with distance from the channel entrance. This effect can produce, however, some mismatch of measured mass flow data and direct velocity data, which are influenced by low velocities in the boundary layer, at positions downstream of the entrance. Calibration coefficients were used to realize a proper fit between mass flow data and direct velocity data. This effect was observed at relatively low velocity values (<100 m/s), and was negligible at high velocity values. In the case of flows in channels the method opens an additional unique possibility of study the boundary layers close to the channel walls.

# 4 Experimental analysis

**Integral mass flow:** The mass flow curves are shown in Fig. 2. The rising part of the curves is called the *Bernoulli* curve; the horizontal parts are the so-called *choked* flow. The inflection

[2]The Reynolds number is defined by $Re = \frac{v \cdot D}{\nu}$. The flow velocity is denoted by $v$, the characteristic length by $D$ and the kinematic fluid viscosity by $\nu$.

| No. | $P_{in}$ [bar] | $P_{out}$ [bar] |
|---|---|---|
| 1 | 300 | 120 |
| 2 | 200 | 80 |
| 3 | 100 | 35 |

| No. | $P_{in}$ [bar] | $P_{out}$ [bar] |
|---|---|---|
| 1 | 300 | 80 |
| 2 | 200 | 50 |
| 3 | 100 | 20 |

Table 1: CCP for I-channel (left) and for Y-channel (right)

points of the mass flow curves are called the cavitation critical points (CCP). The intersection of non-cavitating to cavitating flow is distinguished by the CCP. The position of CCP depends on the pressure difference (for a fixed inlet pressure) and the inflow temperature. The generation of pressure waves and noise, induced by cavitation, reaches a maximum at this point, see [2]. Due to this fact, the CCP is of great interest for the experimental analysis. It depends on the fluid quality, such as nuclei distribution and air content rates, see [8, 7].
The following pressure values for CCP were determined from the experiment, see Fig. 2 and Table 1. The mass flow was measured for three constant inlet pressure values and variable outlet pressure values. The inlet temperature is fixed at 40 °C. Local velocity profiles as well as density and pressure distributions and fluctuations in the throttle domain are of main interest at the CCP.

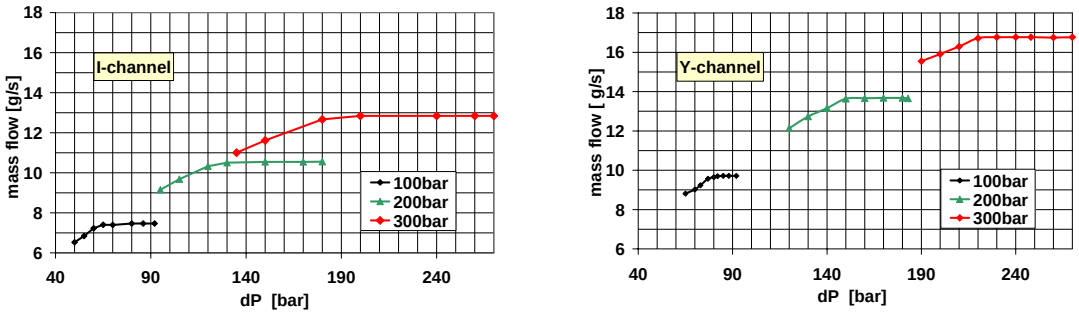


Figure 2: Mass flow curve for inflow pressure $P_{in}$=100 bar (black), 200 bar (green) and 300 bar (red) of I-channel (left) and Y-channel (right)

**Cavitation, density gradients and turbulence visualization:** The uniform liquid areas of the flow remain transparent, but density gradients, turbulent areas and gas bubbles produce a shadow. The dark regions in the images correspond to the gas phase. A light transmission is mainly affected by cavitating gas bubbles. As a rule single spherical bubbles are not detected even at highest optical magnification and resolution and the cavitation looks like arbitrary shaped clouds. The data can be also presented as a result of a statistical evaluation as mean bubble-density or cavitation probability distributions. Examples of these measurements are presented in Fig. 3. In contrast to [1], it is assumed that cavitation bubbles appear directly in the center of vortices. Vortex structures have a great influence on the structure of cavitation which was studied in several publications, cf. [3, 16]
**Local density distributions** were measured using interferometry [12, 13], and corresponding pressure and temperature distributions were calculated using the following formula (Taylor expansion for a function with two independent variables):

$$\rho(p,T) \approx \rho(p_0,T_0) + \frac{\partial\rho}{\partial p}|_{(p_0,T_0)}(p-p_0) + \frac{\partial\rho}{\partial T}|_{(p_0,T_0)}(T-T_0) \tag{1}$$

The approximation is valid for the liquid phase, i.e., $p_D < p$ and $T < T_{si}$[3]. Examples of the density distribution measurements are displayed in Fig. 4 and Fig. 5. Essential density fluctuations are located in the throttle and in the back flow. The mean density gives reason to believe that the

[3] $p_D$ denotes the vapor pressure and $T_{si}$ the saturation temperature

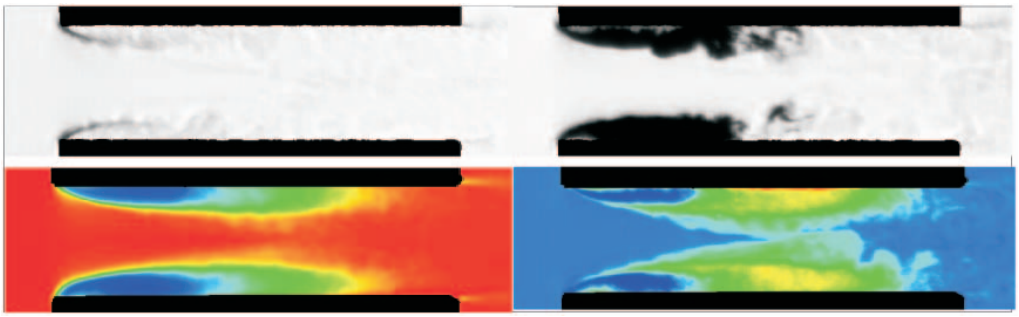

Figure 3: I-channel: Upper Figure (Left): Turbulence and shear layers at $P_{in}$=300 bar, $P_{out}$=165 bar; (Right): cavitation at $P_{in}$=300 bar, $P_{out}$=120 bar. Single transmission images. Light – liquid, dark – gas. Lower Figure (Left): Statistical evaluation, number of images N=50. $P_{in}$=300 bar, $P_{out}$=120 bar: mean cavitation distribution, red – liquid, blue – gas. (Right): fluctuations liquid/gas (RMS), red – high fluctuations, blue – low.

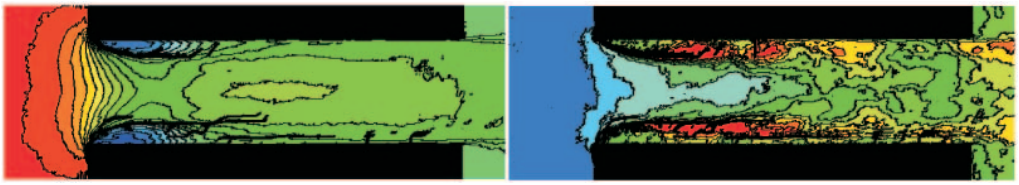

Figure 4: I-channel: Density distribution, $P_{in}$=300 bar, $P_{out}$=165 bar, number of images N=43. (Left): mean density distribution, red – high density, blue – low density. (Right): density fluctuations (RMS), red – high density fluctuations, blue – low.

minimal pressure is at the inlet on the boundaries of the throttle. Cavitation is originally generated in the areas with high pressure fluctuations (shear layers) and then spread out into the areas with low density (pressure) at the recirculation areas.

**Velocity profiles:** The velocity profiles of throttle flows were measured using spatially narrow and temporally delayed LIF-signals, excited by powerful UV-radiation from a KrF-laser. The measurements were performed inside the channels at different cross-sections, and beyond the channel. Examples of the measurement results are presented in Fig. 6 and 7.

**Analysis of experimental data at critical cavitation points:** Hydraulic flow values ($P_{in}$, $P_{out}$, $T_{in}$, $T_{out}$, mass-flow), which were measured with external sensors, remain stable at the critical cavitation points. The pressure values for Critical Cavitation Points are listed in Table 1. The outlet pressure sensor is located far away from cavitation areas so that generated pressure waves by cavitation have disappeared. At the same time optical measurements detect the strong fluctuations of the size of cavitation area inside the channel, corresponding fluctuations of pressure and velocity were also measured. The instability effects were even more pronounced for this channel. Statistically, about 25% of images display cavitation near the inlet only, about 25% images show the cavitation in the complete channel length, and the rest display intermediate lengths of cavitation zones at CCP for the Y-channel. Velocity values at the middle of the Y-channel (see Fig. 6), which correspond to states with long cavitation area, are higher ($\delta v$ =40 m/s at first CCP, see Table 1 for round inlet geometry) than velocity values for states with short cavitation zones. These higher velocities supply the proper mass-flow for a narrow active channel cross-section, which is partially blocked by cavitation, see Fig. 7. In turn, the measured local pressures at the middle of the channel are lower ($\approx$ 70 bar at first CCP for Y-channel) for states with longer cavitation length, i.e., pressure difference between channel inlet and middle is higher for longer cavitation areas.

The measured pressure fluctuations inside channels correspond very well to the velocity fluctuations measured by LIF-technique. The correlation between local statical pressures and local

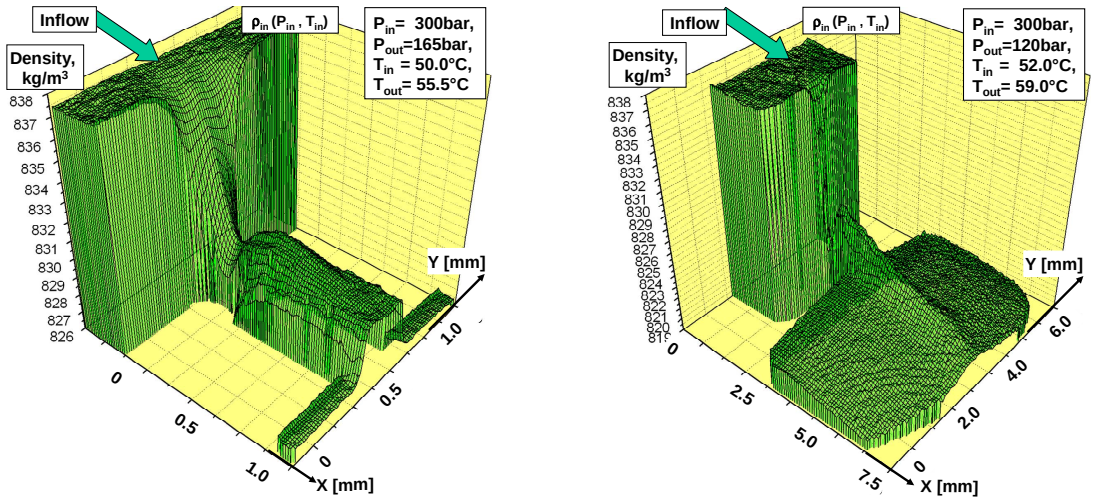


Figure 5: I-channel: Mean density distributions. (Left): N=43. $P_{in}$=300 bar, $P_{out}$=165 bar. Optical magnification 1.1 µm/pix. (Right): N=42. $P_{in}$=300 bar, $P_{out}$=120 bar. Optical magnification 6 µm/pix.

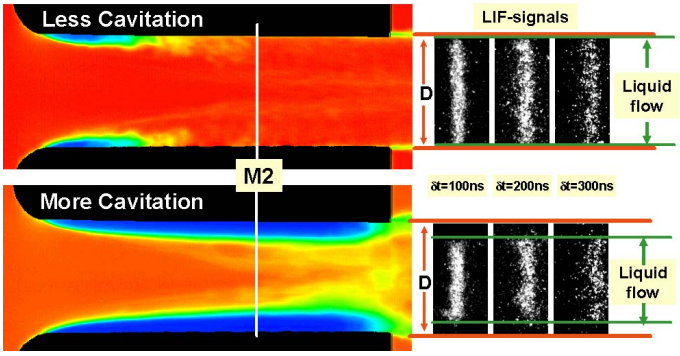


Figure 6: Y-channel: $P_{in}$=300 bar, $P_{out}$=80 bar. (Left): cavitation distributions with small and large cavitation length. (Right): corresponding LIF-signals at position M2.

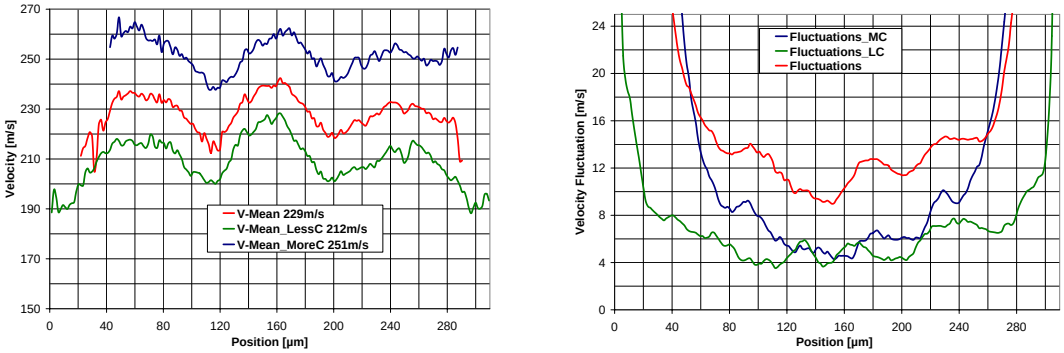


Figure 7: Y-channel: Position M2. Velocity profiles at CCP $P_{in}$=300 bar, $P_{out}$=80 bar. Blue – realization with strong cavitation (N=18), green – weak cavitation (N=17), red – all images (N=100).

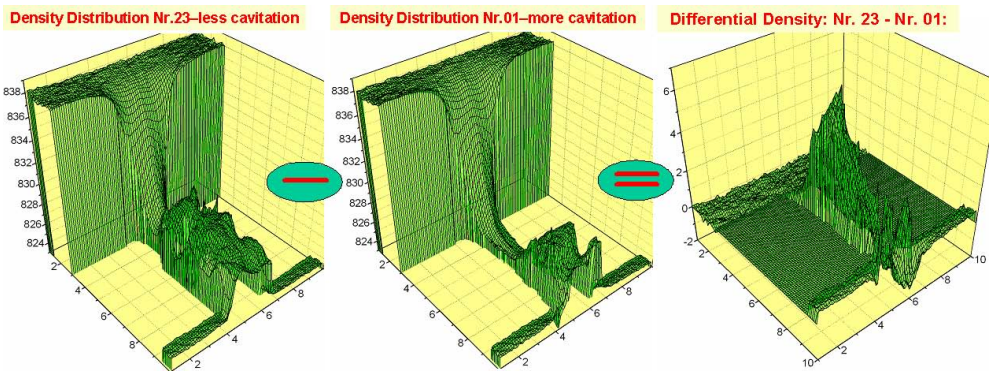


Figure 8: I-channel: Density distributions at critical cavitation point $P_{in}$=300 bar, $P_{out}$=120 bar. (Left): measured realization with small cavitation zone at inlet; (Middle): realization with long cavitation zone; (Right): differential density distribution.

velocities is determined by Bernoulli equation ($p_x + \frac{\rho v_x^2}{2} = \text{const}$, where $x$ is the coordinate along the channel). This correlation between $p_x$ and $v_x$ was proved at all CCP for both round and sharp inlet geometries.

Density distributions at CCP display strong fluctuations which are connected with fluctuations of cavitation area inside the channel. Instances with small cavitation areas display higher density and pressure compared with realizations with long cavitation area. The measured pressure differences between states reach values of 120 bar, which are comparable with outlet pressure at first CCP for sharp inlet geometry. The measured distributions for instances with long cavitation lengths detect very low pressure values inside the channel. These low pressure values provoke cavitation development. These pressure fluctuations are local and very fast at the same time. They are not detected by our external pressure sensors (sampling rate $\approx$50 kHz).

At higher outlet pressures (without cavitation), the pressure fluctuations are generated at the shear layers at the inlet of the channel and behind it, and then go along with main flow downstream. The shot-exposure single-shot differential images display a "frozen" periodical spatial structure of these fluctuations, see Fig. 9. Using the measured spatial period of the fluctuations and the obtained velocity values, on can calculate a fluctuation appearance frequency. These fluctuation frequencies were estimated as 300 kHz – 560 kHz inside the throttle and about 80 kHz – 150 kHz at the free jet area behind the throttle channel using the obtained differential density distributions and velocity profiles.

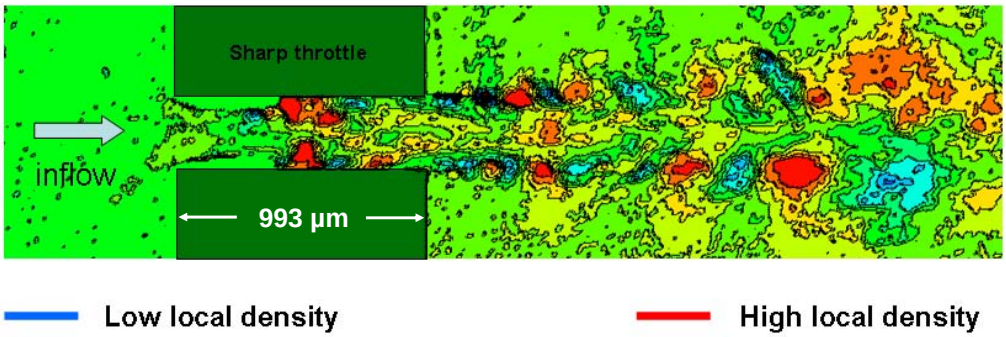


Figure 9: Sharp channel I: Optical magnification 6 µm/pix, $P_{in}$=300 bar, $P_{out}$=165 bar. Differential density distribution: Instant density minus mean distribution.

# 5 Numerical simulations

A three-dimensional simulation of the complete hydraulic system can not be carried out due to the great computational effort. Therefore, a part of the system including the throttle is defined. The throttle geometry is chosen with an inlet and an outlet domain, see Fig. 10. Pressure boundary conditions are defined. The commercial CFD code ANSYS CFX-11.0 is used to simulate the throttle flow. The flow is assumed to be isothermal, i.e., the temperature is fixed and constant. An equation of state $\rho = \rho(p)$ for the Diesel oil based on an experimental data basis[4] is implemented in the simulation code. The default cavitation model is used, i.e., a linearization of the Rayleigh-Plesset equation is used for phase transition. The model parameters for the cavitation model such as vapor pressure and nuclei density have to be determined in separate experiments, [7]. Even though the Diesel fluid is a multi-component fluid, it is assumed that a fixed vapor pressure exist which is defined by 4500 Pa at 40 °C based on experiments. Further, it is assumed for simplicity of the physical models, that both phases have the same velocity and the same pressure – the typical requirements for a homogeneous two-phase flow regime. The computational grid was adapted to the flow. The inflow domain consists of a coarse grid. The throttle domain and the rear of the throttle contain a very fine grid. A coarse grid was used for the outlet domain. The fine grid and the coarse grid are connected with the non-matching General Graphics interface (GGI) given in ICEM, see Fig. 11, so that three separate domains exist. No-slip boundary conditions are used on the steel walls as well as on the window walls. The small grid size guarantees an integral mass flow which is independent of the mesh. It is well known that the turbulence model has a significant influence on the computed cavitation zones and the vortex structures in and behind the throttle. Three different turbulence models were used on a common computational grid: URANS with the SST-model, Scaled Adaptive Simulation (SAS) and WALE-LES model.

*URANS SST:* The simulation model is based on the **U**nsteady **R**eynolds-**A**veraged **N**avier **S**tokes equations in connection with a two-equation turbulence model which is a combination of a $k$-$\epsilon$ and a $k$-$\omega$ model, a special wall function, and a y+-insensitive wall treatment.

*SAS:* The **S**caled **A**daptive **S**imulation using two-equation turbulence models was derived in order to resolve large vortex structures in a URANS simulation. The concept is based on the introduction of the von Karman-length scale into the turbulence scale equation. The information provided by the von Karman-length scale allows SAS model to dynamically adjust to resolve vortex structures in a URANS simulation, for details see [9].

*WALE-LES:* The **L**arge **E**ddy **S**imulation model which is based on the square of the velocity gradient tensor accounts for the effects of both the strain and the rotation rate of the smallest resolved turbulent fluctuations, for details see [10]. In contrast to the SAS model, the turbulent viscosity is calculated by an algebraic equation. This means a smaller computational effort in contrast to URANS-SST or SAS models per control volume, but requires a LES resolution of eventual turbulent wall boundary layers.

Velocity profiles were measured at different positions, which are given in Fig. 12 and compared with simulation results. The focus is on the positions IN1 (in front of the throttle), M2 (inside the throttle) and OUT1 (behind the throttle).

| Method | Time step $\Delta t$ [s] | Number of Time steps | Init. solution | Number of nodes |
|---|---|---|---|---|
| URANS | $10^{-7}$ | 300 | RANS-sol. | $2.48 \cdot 10^6$ |
| SAS | $10^{-8}$ | 3000 | URANS-sol | $2.48 \cdot 10^6$ |
| WALE-LES | $10^{-8}$ | 3000 | URANS-sol. | $2.48 \cdot 10^6$ |

Table 2: Simulation methods and coefficients of simulation methods

Table 2 contains the simulation parameters such as time step size $\Delta t$, the number of computational time steps, the kind of initial solution for the simulations, and the number of nodes.

[4] liquid density $\rho(p = 1\,\text{bar}, T = 293\,K) = 820$ kg/m$^3$, speed of sound $c(p = 1\,\text{bar}, T = 293\,\text{K}) = 1320$ $m/s$, viscosity $\nu = 3.5 \cdot 10^{-6}$ m$^2$/s

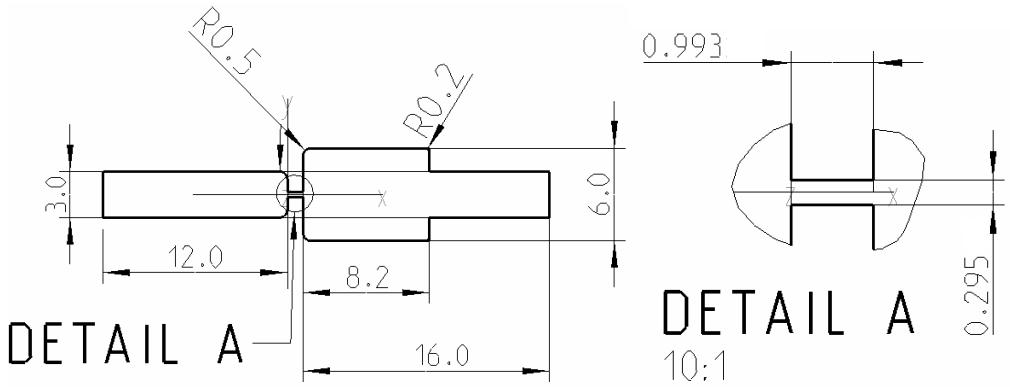


Figure 10: Geometrical data of I-channel: (Left): complete geometry; (Right): detail inlet. Geometrical dimensions in [mm]

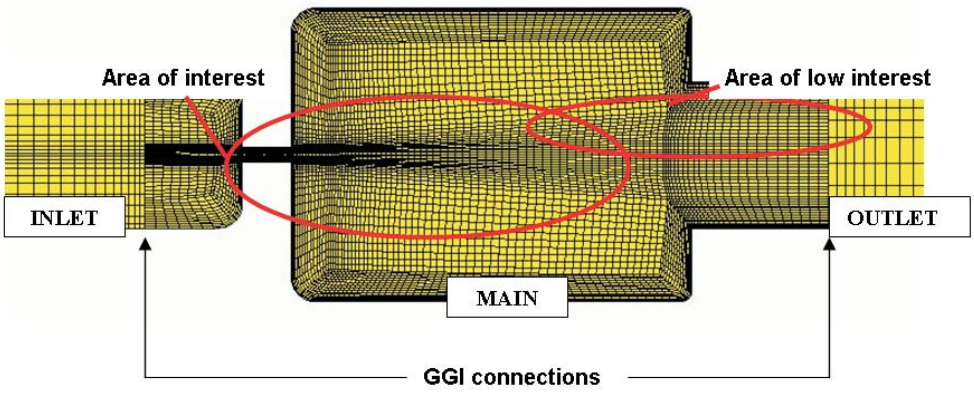


Figure 11: Computational grid for I-channel: Local refinements of the computational grid with General Graphical Interfaces. For geometrical details see Fig. 10.

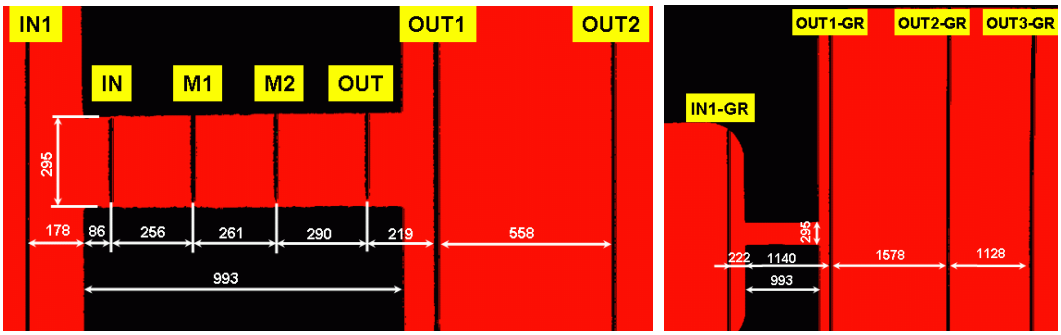


Figure 12: I-channel: Geometrical positions for velocity distribution measurements with LIF. Geometrical dimensions in [$\mu$m]. Velocity profiles at positions IN1, M2, and OUT1 are compared with simulation results

Figure 13: I-channel: (Upper left) Transmitted light, cf. Fig. 3; (Upper right) computed density field (white: liquid) of URANS for pressure difference of 300 bar – 120 bar, (Lower left) SAS and (Lower right) WALE-LES

**Results of numerical simulations:**
*URANS-SST:* The simulation tends to a nearly steady state solution for pressure, velocity and volume fraction fields in and behind the throttle. The typical pressure as well as velocity fluctuations measured in experiments can not be computed by this simulation due its steady character. It leads to a constant mass flow at in- and outlet boundaries. Cavitation at the inlet of the throttle is computed; the shear layer cavitation is not predicted for smaller outlet pressure values. A steady simulation leads to insufficient degrees of residuals.
*SAS:* The simulation tends to a steady state solution in the throttle and a transient solution behind the throttle. The missing laminar separation on the throttle leads to vortex structures with weak pressure fluctuations in the shear layer of the throttle back flow.
*WALE-LES:* The simulation reflects the highly transient properties of the cavitating flow. High pressure as well as velocity fluctuations inside the throttle are predicted. Pressure fluctuations are also predicted in the shear layer. The resolution of vortex structures (laminar separation on the inlet of the throttle) leads to a transient behavior of the velocity profiles at the considered positions.
Due to the low Reynolds number[5] of the flow, the failure of the URANS and the SAS models to produce unsteady structures is not surprising. Both models predict turbulent flow with a high eddy-viscosity already upstream of the separation in contradiction to the experiments. In order to capture the correct flow behavior upstream of the separation, the model would have to be augmented with a transition model. However, for the current flow, the advantage of both URANS and SAS models to avoid the resolution of turbulent boundary layers is not relevant, as turbulence is mostly concentrated in the separated shear layers. Therefore a LES model is more suitable as the shear layer turbulence has to be resolved in any case to capture the unsteady cavitation effects. It should be noted that the WALE model was chosen as the LES closure, as it returns to zero eddy viscosity in laminar shear flows.
**Transmitted light – volume fraction distribution:** The vapor bubble distribution of experiment and simulation is compared in the following. URANS as well as SAS lead to a nearly steady distribution of vapor bubbles inside the throttle. In contrast to this, the WALE-LES leads to a transient distribution of vapor bubbles inside the throttle. The laminar separation areas are thereby filled with vapor bubbles. The computed distribution of vapor bubbles well agree with the experimental results inside the throttle. **Velocity profiles at selected positions:** The velocity profiles measured in experiments for the sharp throttle are compared to the simulation results at position IN1, see Fig. 14. The computed velocity profiles coincide well with the profiles determined by the experiment for both pressure differences. Twenty velocity profiles of consecutive time steps are averaged for representation. The next position is M2 which is located in the throttle. At

[5] $Re_{inflow} \leq$2100 and $Re_{throttle} \leq$18000 for sharp and rounded throttle geometry

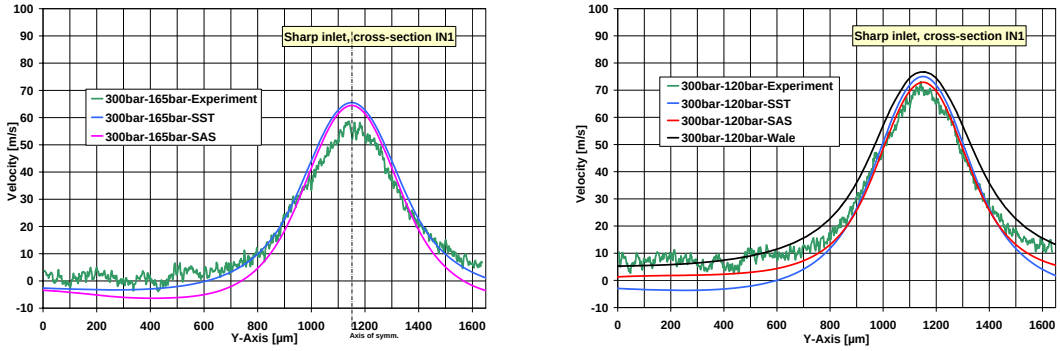


Figure 14: Position IN1: Velocity profiles for pressure differences 300–165 bar and 300–120 bar for URANS-SST, SAS and WALE-LES in the comparison with the experiment

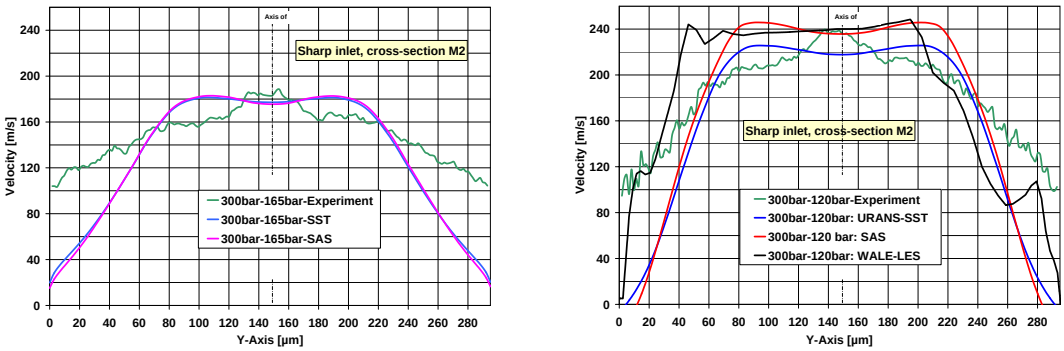


Figure 15: Position M2: Velocity profiles for pressure differences 300–165 bar and 300–120 bar for URANS-SST, SAS and WALE-LES (middle value of 30 consecutive time steps) in comparison with the experiment

this position larger differences between experiment and simulation appear, cf. 15. The differences occur near the lower and upper wall. Note that cavitation appears at the corner of the throttle which has an influence on the flow field at position M2. A short over prediction of the maximal velocity values is the result of the comparison between experimental and simulation results.
Three major causes are identified for the differences between experimental and simulation results. They are listed by importance.

- A problem in comparison between simulation and experiments is the different statistics of the reporting. Let us consider the experimental data for analysis of density fluctuations in the experiments. Approximately 50 images of density are taken in a period of 100 ms by an exposure time of 400 ns. The mean pressure values are computed as well as the RMS. The images are statistically independent over a period of $\approx 5$ seconds. The period of 100 ms is limited by the camera. Fast fluctuations ($\omega$>2 MHz) are averaged during 400 ns and are not visible in experiments. The time steps of the simulations are 10 ns, which is 40 times less than the experimental exposure time. However, the complete simulation time is only 0.03 ms due to the great computational effort[6]. Thus, a direct statistical comparison of results is difficult at the moment.

- The laminar dynamic viscosity of the mixture $\nu$ (liquid-vapor) has an influence on the local pressure loss in the flow and consequently on the vortex structures. Four models for effective viscosity (mixture viscosity) are established, cf. [5]:
  – A convex linear combination of the viscosity of liquid and pure vapor on the basis of volume

[6]The simulation was done on a Linux–cluster with 20 processors.

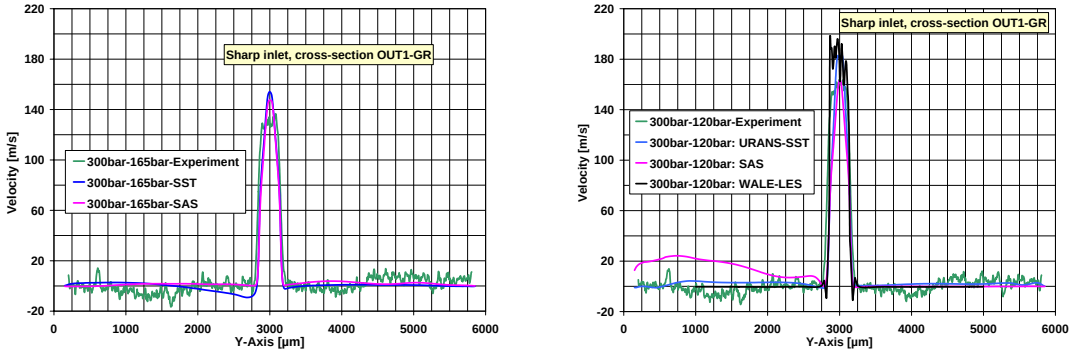


Figure 16: Position OUT1: Velocity profiles for pressure differences 300–165 bar and 300–120 bar for URANS-SST, SAS and WALE-LES (middle value of 20 consecutive time steps) in comparison to the experiment

fraction $\epsilon$[7], i.e., $\nu = (1-\epsilon)\cdot\nu_L + \epsilon\cdot\nu_G$ . This approach is used in the commercial software ANSYS CFX-11.0.
– A combination of the viscosity of liquid and pure vapor on the basis of mass fraction $\mu$, i.e.,

$$\frac{1}{\nu} = \frac{\mu}{\nu_G} + \frac{1-\mu}{\nu_L}.$$

– A combination of the viscosity of liquid and pure vapor based on volume fraction $\epsilon$ and a modeling factor, i.e., $\nu = \epsilon\cdot\nu_G + (1-\epsilon)(1+2.5\epsilon)\cdot\nu_L$
– A theoretical solution of dilute bubble suspension, i.e., $\nu = (1+\epsilon)\cdot\nu_L$.
Further models for effective viscosity of two-phase flow are derived in [4]. It is supposed, that the frequencies of laminar separation with phase transition are directly depend on the viscosity model of the homogeneous mixture.

- The physical flow values of density and pressure are depth-averaged in the experiments. This was not done in numerical simulations because the depth-averaging procedure is not available in the software. The application of these different approaches in ANSYS CFX-11.0 should be validated in a next step. Thus, the comparison of experimental and simulation results is not completely coincident.

# 6 Summary

Detailed experimental investigations have shown the complex structure of cavitating flow, especially near the cavitation critical point. Cavitation generates significant pressure fluctuations as well as a pulsating flow in and downstream of the throttle. The fluctuations continue in the free jet behind the throttle. The measured pressure fluctuations inside the throttle reach values of the outlet pressure at the CCP, which is a completely new knowledge of cavitating throttle flow. The corresponding flow velocity fluctuations due to cavitation inside channels were detected with LIF-measurements.
At the elevated outlet pressures and single-phase liquid flow, the pressure fluctuations are generated at the shear layers and then go along with main flow downstream. These local pressure fluctuations have frequencies of up to 500 kHz and can only be measured by optical measurement techniques. Further, the application of interferometry as well as laser induced fluorescence guarantees detailed validation data for the numerical simulation.
Three different turbulence modeling concepts for homogeneous two-phase flow available in the commercial CFD code ANSYS CFX-11.0 were applied. The well-known URANS as well as the

[7]Index $G$ denotes the gas phase, $L$ the liquid phase.

SAS models lead to a nearly steady state solution for the flow field inside the throttle. The SAS resolves the shear layer flow of the free jet behind the throttle. Only the WALE-LES approach can resolve the laminar separation in combination with phase transition at the inlet of the throttle as well the large vortices in the shear layer of the free jet. This is not surprising, as large portions of the flow are laminar due to the low Reynolds number of the device. Both URANS and SAS models predict turbulent flow upstream of separation in contradiction with the experiments. The resulting, large eddy viscosity produced by these models suppresses the unsteady nature of the flow. For such low Reynolds number flow, the LES approach is therefore the most appropriate turbulence closure. This method requires the smallest computational effort in contrast with the other tested methods on a fixed computational grid and per time step. The large computational time on fine grids does not allow long simulation times for a detailed statistical report of physical values such as pressure distribution or velocity profiles at fixed positions.

**Acknowledgment** The authors would like to thank Dr. F. Menter and Dr. Y. Egorov from ANSYS CFX-11.0 for the fruitful discussions and hints.

# References

[1] H. Alehossein and Z. Qin. Numerical analysis of Rayleigh-Plesset equation for cavitating water jets. *Int. J. Numer. Meth. Engng*, 72:780–807, 2007.

[2] T. Aoyama, S. Suzuki, A. Kawamoto, and T. Noda. *Preventive Design and Analysis of Cavitation Noise on Diesel engine*, 2007. Research Report, Review of Toyota CRDL, Vol. 40, No.1.

[3] T. Baur and Köngeter. *The three-dimensional character of cavitation structures in a turbulent shear layer*, 1998. XIX IAHR Intern. Symp. on Hydr. Mach. and Cav.

[4] D. Bedeaux. The effective shear viscosity for two-phase flow. *Physica*, 121:345–361, 1983.

[5] K. Fukagata, N. Kasagi, P. Ua-arayaporn, and T. Himeno. Numerical simulation of gas-liquid two-phase flow and convective transfer in a micro tube. *Int. J. Heat Fluid Flow*, 28:72–82, 2007.

[6] D. Greif, A. Morozov, E. Winklhofer, and R. Tatschl. *Experimental and Numerical Investigation of Erosive Effects due to Cavitation within Injection Equipment*, 2005. In: Proceedings of 4th ICCHMT, Paris-Cachan, May 17-20.

[7] W. Heller. *Hydrodynamische Effekte unter besonderer Berücksichtigung der Wasserqualität und ihre Messverfahren, Strömungsmechanik, Band 2.* Der Andere Verlag, Tönning, Lübeck und Marburg, 2006.

[8] H. Kamiirisa. *The effect of water quality characteristics on cavitation noise*, 2001. CAV, Session A2.004.

[9] F.R. Menter and Y. Egorov. A scale-adaptive simulation model using two-equation models. 2005. 43rd AIAA Aerospace Sciences Meeting and Exhibit, 10-13 January, Reno, Nevada.

[10] F. Nicoud and F. Ducros. Subgrid-scale stress modelling based on the square of the velocity gradient tensor. *Flow, Turbulence and Combustion*, 1999.

[11] T.J. O'Hern. *Cavitation inception in a turbulent shear flow.* Mechanical Engineering Department, California Institute of Technology, Pasadena, CA, 88-3680-CP.

[12] M. Takeda, H. Ina, and S. Kobayashi. Fourier transformation method of fringe pattern analysis for computer based topography and interferometry. *J.Opt.Soc.Am. 72*, 156, 1981.

[13] E. Winklhofer, E. Kelz, and A. Morozov. *Basic flow processes in high pressure fuel injection equipment.* 9th Int. Conf. On Liquid Atomization and Spray Systems: ICLASS-2003, Sorrento, Italy, 13-18.07.2003. 14-9.

[14] E. Winklhofer, E. Kull, E. Kelz, and A. Morozov. *Comprehensive hydraulic and flow field documentation in model throttle experiments under cavitation conditions.* ILASS - Europe 2001, Zurich, Switzerland, September 2001.

[15] E. Winklhofer, H. Philipp, A. Hirsch, and A. Morozov. *Cavitation and Spray Formation in Diesel Flow Situations*, 2000. ILASS-Europe, Darmstadt, Germany, pp.1.7.1-1.7.6.

[16] K. Yokota, K. Mitsuda, Y. Tsujimoto, and C. Kato. A study of vortex structure in the shear layer between main flow and swirling backflow. *JSME International Journal*, 47:541–548, 2004.